MP-69-P-45

Forebody Aerodynamics of the F-18 High Alpha Research Vehicle With Actuated Forebody Strakes

by David F. Fisher and Daniel G. Murri

Prepared for the Symposium on
Advanced Flow Management

May 7–11, 2001

Loen, Norway

Forebody Aerodynamics of the F-18 High Alpha Research Vehicle With Actuated Forebody Strakes[*]

David F. Fisher
NASA Dryden Flight Research Center
Edwards, CA 93523-0273

Daniel G. Murri
NASA Langley Research Center
Hampton, VA 23681-2199

ABSTRACT

Extensive pressure measurements and off-surface flow visualization were obtained on the forebody and strakes of the NASA F-18 High Alpha Research Vehicle (HARV) equipped with actuated forebody strakes. Forebody yawing moments were obtained by integrating the circumferential pressures on the forebody and strakes. Results show that large yawing moments can be generated with forebody strakes. At a 50°-angle-of-attack, deflecting one strake at a time resulted in a forebody yawing moment control reversal for small strake deflection angles. However, deflecting the strakes differentially about a 20° symmetric strake deployment eliminated the control reversal and produced a near linear variation of forebody yawing moment with differential strake deflection. At an angle of attack of 50° and for 0° and 20° symmetric strake deployments, a larger forebody yawing moment was generated by the forward fuselage (between the radome and the apex of the leading-edge extensions) than on the radome where the actuated forebody strakes were located. Cutouts on the flight vehicle strakes that were not on the wind tunnel models are believed to be responsible for deficits in the suction peaks on the flight radome pressure distributions and differences in the forebody yawing moments.

NOMENCLATURE

ANSER	actuated nose strakes for enhanced rolling
C_{n0}	aircraft yawing moment at $\beta = 0°$
$C_{n0,\,fb}$	forebody (F.S. = 60 to 190) yawing moment at $\beta = 0°$ from integrated pressures
C_p	pressure coefficient, $(p - p_0)/q_\infty$
CFD	computational fluid dynamics
F.S.	fuselage station, in.
HARV	High Alpha Research Vehicle
HATP	High-Alpha Technology Program
M	Mach number
p	local pressure, lb/ft^2 (Pa)

---

[*] Notice: Use of trade names or names of manufacturers in this document does not constitute an official endorsement of such products or manufacturers, either expressed or implied, by the National Aeronautics and Space Administration.

p_0	free-stream static pressure, lb/ft^2 (Pa)
q_∞	free-stream dynamic pressure, lb/ft^2 (Pa)
Re_c	Reynolds number based on a mean aerodynamic chord of 11.525 ft (3.51 m)
y/b	strake span location divided by the local strake span
α	aircraft angle of attack, deg (from left wingtip angle-of-attack vane, corrected for upwash and boom bending)
β	aircraft angle of sideslip, deg (average of left- and right-wingtip sideslip vanes, corrected for angle of attack)
$\Delta C_{n\,-30^\circ rud}$	incremental change in aircraft yawing moment coefficient due to a –30° deflection of both rudders
δ_s	single strake deflection, deg
$\delta_{s,d}$	differential strake deflection, right strake deflection minus left strake deflection, deg
$\delta_{s,\,L/R}$	left and right strake deflection measured from the retracted position, deg
θ	forebody cross-section circumferential angle, deg (0° is bottom centerline, positive is clockwise as seen from a front view, 0° to 360°)

INTRODUCTION

The NASA High-Alpha Technology Program (HATP) was initiated to increase understanding, improve prediction techniques, provide design guidelines, and investigate new concepts for controls effectors on advanced, highly maneuverable aircraft at high angles of attack.[1] This program used the F-18 configuration as a validation and demonstration vehicle. The flight vehicle consisted of a highly modified F-18 referred to as the High Alpha Research Vehicle (HARV).[2] The HATP consisted of wind-tunnel tests of subscale and full-scale models and components, calibration of computational fluid dynamics (CFD) codes, piloted simulations, and full-scale flight testing. New ground test, CFD, and flight test results were obtained and techniques were developed as a result of this program. These results and techniques were summarized in several high angle of attack conference publications.[3-6]

Several new concepts for control at high angles of attack have been investigated in the wind tunnel and with CFD. Such concepts include engine thrust vectoring[7] and forebody vortex control using actuated forebody strakes[8,9] and pneumatic blowing.[10,11] An in-flight closed-loop thrust-vectoring system has been installed on the HARV, and the results have been documented.[12] More recently, closed-loop actuated forebody strakes were installed, and the results are reported in the proceedings of the 1996 high angle of attack conference.[6] Although not a part of HATP, an open-loop pneumatic blowing flight control system was flight-tested on the X-29A airplane at high angles of attack.[13,14]

This paper examines the local flow aerodynamics of the forebody strakes and their effect on the forebody aerodynamics of the aircraft. Local forebody pressure distributions and forebody yawing moment results obtained on the F-18 HARV during the Actuated Nose Strakes for Enhanced Rolling (ANSER) program are presented. The ANSER acronym refers to “rolling” because the strakes provide the critical yaw control required to coordinate rolling maneuvers about the velocity vector at high angle of attack (α, alpha) conditions.[15,16] Forebody yawing moments are presented for maximum single strake deployments for $\alpha = 20°$ to 65°. Forebody yawing moments and pressure distributions are presented at $\alpha = 50°$ for two symmetric strake deployments. Comparisons with ground facility results for a full-scale F-18 model are included. A more comprehensive presentation of the results in this paper is available as reference 17.

EXPERIMENT DESCRIPTION

The following sections describe the vehicle instrumentation, data reduction and test conditions used in these experiments.

Vehicle Description

Figure 1 shows the F-18 HARV. This highly modified full-scale development twin-engine, single-place, fighter/attack (F/A) airplane was originally built for the U.S. Navy by the McDonnell Douglas Corporation (St. Louis, Missouri) and the Northrop Corporation (Newbury Park, California). The F-18 HARV is powered by two modified General Electric (Lynn, Massachusetts) F404-GE-400 afterburning turbofan engines rated at approximately 16,000 lbf of static thrust at sea level.

The F-18 HARV features a midwing configuration with a wing-root leading-edge extension that extends from the forward portion of the fuselage and blends into the wing. The F-18 HARV carries no stores or missiles and is highly instrumented for research purposes. The wingtip launching rails and missiles were replaced with specially designed camera pods and airdata sensors.[18] More specific details of the F-18 HARV can be found in reference 2.

The HARV was modified by adding externally mounted engine thrust vanes for the deflection of the exhaust to provide additional pitching and yawing moments. The engines were modified to accommodate the thrust-vectoring vane installation by removing the divergent flap portion of the nozzle. The thrust-vectoring capability was provided by controlled deflection of the vanes (three for each engine), which moved into the engine exhaust plume.[2]

For the ANSER program, a new radome was fabricated at NASA Langley Research Center, Hampton, Virginia, that incorporated hydraulically operated conformal actuated forebody strakes. Figure 2 shows a schematic of the strakes. These strakes are 48 in. (1.22 m) long and are positioned longitudinally 120° up from the bottom of the forebody beginning at 8 in. (20 cm) aft of the forebody apex. Figure 3 shows the airplane with the right strake (pilot view) deployed at 90°. When the strakes are closed, there are no protrusions, and the external mold line of the radome conforms to the original radome shape.

Instrumentation

The fuselage forward of the cockpit was extensively instrumented with surface pressure measurements (fig. 4). Five circumferential rings of pressure orifices were installed on the surface of the radome and forward fuselage, forward of the cockpit canopy at fuselage station (F.S.) 70, F.S. 85, F.S. 107, F.S. 142, and F.S. 184. On each forebody strake, three rows of orifices were installed on the outboard surface at F.S. 70, F.S. 85, and F.S. 107, and two on the inboard surface at F.S. 85 and F.S. 107. In addition, three rows of orifices (F.S. 70, F.S. 85, and F.S. 107) were installed on the cove section of the forebody. This region of the forebody is exposed when the strake is actuated. The forebody pressures were measured with a ±216 lbf/ft^2 (10.3 kPa) differential pressure transducer, and the strakes used ±720 lbf/ft^2 (34.5 kPa) transducers. The accuracy was estimated to be ±1 lbf/ft^2 (48 Pa) for the forebody pressures and ±3 lbf/ft^2 (144 Pa) for the strake pressures. More detailed information of the instrumentation has been given previously.[19]

Airspeed, altitude, angle of attack (α) and angle of sideslip (β) were measured using airspeed booms mounted on specially designed wingtip photograph pods. A swiveling probe that was designed with four vanes to align the pitot-static probe head with the local airstream was on the left wingtip.[18] Aircraft angle of attack was measured by using a vane on the left wingboom and corrected for upwash and boom bending. Angle of sideslip was determined as the average of the left- and right-wingboom sideslip vane measurement corrected for angle of attack.

Data from these measurements, as well as from the standard aircraft control positions, inertial systems, and accelerometer parameters, were transmitted to a ground station. These critical parameters were monitored by engineers and technicians in real time on strip charts and displays. These data were monitored in real time at NASA Dryden Flight Research Center, Edwards, California, and Langley Research Center, Hampton, Virginia.

On selected flights, smoke flow visualization was used to mark and identify the off-surface forebody/strake vortical flows. For these flights, the nose cap on the ANSER radome was replaced with one that had two 1.0-in. (2.54-cm)-diameter smoke ports, placed symmetrically 60° up from the bottom centerline. Figure 5 shows a closeup of the right smoke port and radome after a flight. White smoke from a smoke generator system[20] used previously[21] on the F-18 HARV was fed from the smoke generator system through a single 1.5-in. (3.81-cm)-diameter tube to the two 1.0-in. (2.54-cm)-diameter symmetrically located ports on the nose cap. Also shown in figure 5 are six cutouts on the lower portion of the right strake that provided clearance for the radome bulkheads. These cutouts will be discussed later in Results and Discussion.

DATA REDUCTION TECHNIQUES

For the forebody and strake pressures, in-flight zero differential pressures were taken before each test point and were used in postflight data reduction to correct the data for calibration offsets. Time segments of 1.0-sec duration were used for data analysis purposes with approximately 25 time points averaged.

Forebody yawing moment coefficients were determined by integrating the five rings of pressures on the forebody, the pressures on the coves, and the pressures on the strakes over their respective projected forebody side areas. For the forebody, this area extended from the forebody apex to the apex of the wing leading-edge extensions. Pressures were integrated for flight conditions in which the angle of sideslip was less than ±0.5° to determine the yawing moment at 0° sideslip.

During data analysis, pressure coefficients were noted on the lower fuselage centerline that were greater than 1.0 during extremely high-angle-of-attack flight, $\alpha \geq 60°$. This anomaly had not been noted in earlier flight tests.[19,22] At these angles of attack, the aircraft is no longer able to maintain constant altitude. In fact, the aircraft descended at a rate of 200–300 ft/sec. During subsequent hangar tests of the swiveling probe pitot- and static-pressure orifices, an approximate 0.3-sec lag was noted. Possibly, the flexible pressure tubing for the swiveling probe pitot and static pressures had become restricted as compared to previous flight data. For the flight conditions of the data within this paper, ($M \leq 0.4$ and altitudes near 25,000 ft (7,620 m)), this lag was estimated to be approximately 0.6 sec after adjusting for the change in density and viscosity at altitude.[23] Therefore, for these results, the pitot static data were time-skewed by 0.6 sec.

FLIGHT TEST CONDITIONS

Data were obtained in quasi-stabilized 1-*g* flight maneuvers at a nominal altitude of 25,000 ft (7,620 m) and $M \leq 0.4$ for $\alpha = 20°$ to $65°$. At angles of attack greater than approximately 30°, constant altitude could not be maintained, and these data were obtained in a descent. The pressure distribution data were obtained during open-loop flight maneuvers, and the flow visualization data were obtained during open- and closed-loop maneuvers. For the data presented, with few exceptions, $|\beta| \leq 0.5°$.

RESULTS AND DISCUSSION

This section first discusses the forebody yawing moments to show the overall effect of the forebody strakes. The forebody and strake pressure distributions are then presented to explain a forebody yawing moment reversal. Flow visualization is used to support the interpretation of the pressure distributions. Finally, pressure distributions from a full-scale wind tunnel model are presented for comparison.

Forebody Yawing Moments

Figure 6 shows the yawing moment at 0° sideslip from the 30- by 60-ft[24] and 80- by 120-ft[25] Wind Tunnels for the complete airplane. Data are presented as a function of angle of attack for left and right strake deflections, $\delta_{s,\,L/R} = 90°/0°$, $0°/0°$, and $0°/90°$. Figure 6 also shows yawing moments for just the forebody alone (F.S. 60 to F.S. 190) from flight and the 80- by 120-ft Wind Tunnel. Note that when the left strake is deflected, 90°/0°, the yawing moment is positive or to the right and the converse is true when the right strake is deflected, 0°/90°. This same figure shows the strong effectiveness of the actuated forebody strakes at high angle of attack, especially when compared to the rudder. The maximum forebody yawing moment from flight is approximately one-half of the total maximum aircraft yawing moment from the wind tunnels. At $\alpha = 50°$ the flight forebody yawing moment is approximately 80 percent of the wind-tunnel value. The peak forebody yawing moment from flight was at $\alpha = 55°$ and at $\alpha = 59°$ (maximum test α) for the wind tunnel. For the whole airplane, the maximum yawing moment was at $\alpha = 50°$. At $\alpha = 59°$ for the wind tunnel and $\alpha = 65°$ for flight, the forebody and total aircraft yawing moments were approximately equivalent. The differences between the flight and wind-tunnel forebody yawing moments will be discussed further in the Pressure Distributions subsection.

During development in wind-tunnel tests,[16] deflecting one strake at a time, fig. 7(a), at high angles of attack could result in a small but undesirable control reversal at small strake deflections. To overcome this undesirable characteristic for closed-loop control, a solution was developed that deploys the strakes symmetrically as angle of attack increases to $\alpha = 30°$ and greater. When a yawing moment is desired under these conditions, the strakes are deflected differentially about a symmetric strake deployment . For example, using the 20° symmetric strake schedule, (fig. 7(b)), $\delta_{s,d} = 0°$ would correspond to $\delta_{s,\,L/R} = 20°/20°$, $\delta_{s,d} = 10°$ would correspond to $\delta_{s,\,L/R} = 15°/25°$, $\delta_{s,d} = 20°$ would correspond to $\delta_{s,\,L/R} = 10°/30°$ and so on. For all angles of attack, however, the maximum yaw control deflection would always consist of one strake fully deployed (90°) and the other strake fully retracted (0°).

Figure 8 shows the forebody yawing moments from flight as a function of differential strake deflection, $\delta_{s,d}$, (right strake deflection minus the left strake deflection). At $\alpha = 50°$, these data show the variation of forebody yawing moment with differential strake deflection for the 0° and 20° symmetric strake deployments. For the 0° symmetric strake deployment, the left and right strakes are at 0° (closed) when no yawing moment is desired. For the 20° symmetric strake deployment, the left and right strakes are deployed symmetrically to 20° when no yawing moment is desired. The 0° symmetric strake deployment results in a large control reversal. The 20° symmetric deployment eliminates the control reversal and results in a nearly linear variation of forebody yawing moment for differential strake deflections.

For comparison, figure 9 shows the forebody yawing moments at $\alpha = 50°$ for the 0° and 20° symmetric strake deployments from the 80- by 120-ft Wind Tunnel. As compared with the flight forebody yawing moments, the yawing moment reversal for the 0° symmetric strake deployment from the wind tunnel is only about one-half the flight value (fig. 8). The 20° symmetric strake deployment is much improved but not quite as linear as the flight case. The maximum forebody yawing moments from the wind tunnel at $\delta_{s,d} = \pm 90°$ is approximately 25-percent higher than the flight values. The explanation for these differences will be given later under the Pressure Distributions subsection.

In figure 10, the flight forebody yawing moments at $\alpha = 50°$ are broken down into two parts for the 0° and 20° symmetric strake deployments: the ANSER radome including strakes (F.S. = 60 to 124.5) and the forward fuselage between the radome and the apex of the wing leading-edge extension (F.S. = 124.5 to 190). For the 0° symmetric strake deployment, the majority of the yawing moment results from the side force on the forward fuselage, including the region of yawing moment reversal, $|\delta_{s,d}| < 30°$ (fig. 10(a)). Using the 20° symmetric strake deployment, the yawing moment reversal is no longer present for the radome and the forward fuselage (fig. 10(b)). Again, as for the 0° symmetric strake schedule, the strakes generate little yawing moment at $|\delta_{s,d}| < 30°$ as shown by the radome data. However, the vortices the strakes generate create a significant yawing moment further aft on the forward fuselage. Approximately 80 percent of the forebody yawing moment for $|\delta_{s,d}| \leq 30°$ at $\alpha = 50°$ is caused by the side forces on the forward fuselage. At $\delta_{s,d} = \pm 90°$ the forward fuselage accounts for 55 to 60 percent of the forebody yawing moment.

Pressure Distributions

Figure 11 shows the forebody and deployed strake pressure distributions for $\alpha = 50°$ for the 0° and 20° symmetric strake deployments. This figure shows the aerodynamic mechanisms responsible for the yawing moments generated by the strakes. For the 0° symmetric strake deployment, large yawing moment reversals were present. For the 20° symmetric strake deployment, the yawing moments were linear. Separate plots are shown for the forebody and the right and left strakes. Note that the pressure distributions are offset by $C_p = 1.0$ for each consecutive fuselage station for clarity.

0° Symmetric Strake Deployment

Figure 11(a) shows the forebody pressure distributions as a function of the forebody cross-section circumferential angle, θ. The scale for the circumferential angle is reversed so that the pressure distributions can be viewed in the pilot's perspective. The $\theta = 0°$ and 360° are on the lower centerline; $\theta = 180°$ is on the top centerline; $\theta = 90°$ is on the right side of the fuselage; and $\theta = 270°$ is on the left. This convention was established in previous papers.[19,22] The symbols and solid curve indicate the pressure distribution from the HARV ANSER radome. The footprints of the forebody vortices can be seen by the suction peaks in the pressure distributions at $\theta \approx 160°$ and 200° for F.S. 85, F.S. 107, F.S. 142, and F.S. 184. The large suction peaks at $\theta \approx 90°$ and 270° for F.S. 70, F.S. 85, and F.S. 107 are caused by the acceleration of the flow around the fuselage that is nearly circular in cross-section. The small suction peak for F.S. 142 at $\theta \approx 110°$ and 250° is caused by a small antenna cover just forward of F.S. 142. The dashed curve indicates pressure distribution data obtained from the original HARV radome.[19] The most obvious difference between ANSER radome results and the original HARV radome results is the deficit in the suction peak at $\theta \approx 80°$ to 110° and 250° to 280°, starting at F.S. 70 and progressing aft to F.S. 107. The original HARV radome suction peak is much smoother and fuller. This deficit region is below the strake. The joint at $\theta \approx 280°$ (where the white and black paint meet below the strake) (fig. 3) could cause boundary-layer transition. Previously, however, boundary-layer transition trips very near this location on the original HARV radome[26] did not show a deficit in this region but did show the enhanced vortex footprints at F.S. 85. The radome was checked for roundness in this region at F.S. 70 and F.S. 85, and the local curvature appeared to be satisfactory. When the radome was fabricated, the strakes were sealed from the interior of the radome and from top to bottom. However, the gap between the retracted strake and fuselage was on the order of 0.1 (0.25 cm) to 0.2 in. (0.5 cm) and large cutouts existed as shown previously in figure 5. Some of these cutouts were 1- by 1-in. (2.5- by 2.5-cm), and some were 1.5- by 2-in. (3.8- by 5.1-cm). This deficit in the suction peak will be discussed further when the ANSER radome pressure distributions are correlated with the 80- by 120-ft Wind-Tunnel model pressure distributions.

Figure 11(b) shows the pressure distributions at $\alpha = 50°$ for the right strake extended to 20°. At this strake deflection a strong yawing moment reversal with the yawing moment positive (or to the right) occurred (fig. 8). At this angle of attack and strake deflection, the pressure distributions become asymmetric with large suction peaks at $\theta \approx 160°$ for F.S. 85 and F.S. 107 caused by the right forebody/strake vortex. The right vortex footprints at F.S. 142 and F.S.184 are diminished because the right vortex is beginning to lift from the forebody surface. The pressures on the right forebody tend to be less than those on the left forebody, particularly at F.S. 142 and F.S. 184. Pressures on the strake are less than ambient, and the outboard surface pressures are generally less than the inboard surface pressures. The suction peak on the inboard surface at $y/b = 0.85$ at F.S. 85 is approximately the same magnitude ($C_p \approx -1.2$) as the one on the right forebody and is caused by the proximity to the right forebody/strake vortex. The combination of the forebody and strake pressures results in a yawing moment to the right, not the desired direction.

When the right strake extends to 60° (fig. 11(c)), the forebody pressures on the left side at $\theta = 240°$ to 300° are noticeably less than the corresponding pressures on the right side for all pressure orifice stations, resulting in a yawing moment to the left. At this strake deflection, the strake is approximately 30° out from vertical and retards the flow on the right forebody below the strake. Greater than ambient pressures can be seen on the outboard strake surface at the intersection with the forebody, $y/b \approx 0.2$. The right strake suction peak is a maximum at $\theta \approx 160°$, F.S. 85, and quickly diminishes moving aft as the right forebody/strake vortex lifts from the surface of the radome. The left forebody vortex grows in strength, stays close to the surface, and causes the flow to accelerate around the left side of the forebody. This vortex action results in lower pressures on the left side, hence a yawing moment to the left. The left vortex suction peak is a maximum at $\theta \approx 200°$ at F.S. 107 and moves inboard progressing aft, so this peak is at $\theta \approx 180°$ at F.S. 184. On the strake, pressures on the outboard surface are greater than those on the inboard surface, resulting in a yawing moment to the left. The suction peak ($C_P \approx -2.0$) on the outboard strake surface at F.S. 70, $y/b = 0.85$, is almost the same as for the right vortex suction peak ($C_p \approx -2.1$) at F.S. 85, suggesting that the forebody/strake vortex passes close to that orifice. The sum of large pressure differences on the forebody and strake results in a large yawing moment to the left, (figs. 8 and 10(a)).

When the right strake is fully extended to 90° the strake retards the flow below the strake even more than for $\delta_s = 60°$ (fig. 11(d)). The suction peaks at F.S. 70, F.S. 85, and F.S. 107 and $\theta = 60°$ to 120° are significantly lower than for $\delta_s = 60°$. Pressures on the left side of the fuselage are approximately the same as for $\delta_s = 60°$. On the strakes at F.S. 85, the difference between the inboard and outboard surface pressures is significantly larger than for $\delta_s = 60°$. Like the $\delta_s = 60°$ case, the pressure distributions indicate that the right vortex lifts from the surface after F.S. 85 while the left vortex stays close to the surface and accelerates the flow around the left side. The suction peak ($C_p = -1.9$) on the inboard strake surface at F.S. 85, $y/b = 0.65$, is almost the same as on the fuselage at the same fuselage station. As a result of the lower suction peaks on the forebody and the outboard and inboard surface pressures on the strake at F.S. 85, the yawing moment to the left was even larger than for $\delta_s = 60°$, (figs. 8 and 10(a)).

Figure 12 provides supporting evidence of this interpretation, as shown in the wingtip photograph $\alpha = 50°$, $\beta \approx 0°$, and $\delta_{s,\,L/R} = 0°/90°$. The right forebody/strake vortex can be seen very high off the forebody, departing the surface at the strake. A weaker left forebody vortex can be seen lower and near the surface of the forebody. Dashed lines are used to help identify the vortex paths for the reader.

20° Symmetric Strake Deployment

As discussed previously, symmetric strake deployments were used at high angles of attack to overcome the problem of yaw control reversal at small strake deflections. At $\alpha = 50°$, the 20° symmetric strake deployment yielded good control linearity characteristics (fig. 8).

Figure 13 shows pressure distribution for the 20° symmetric strake deployment at $\delta_{s,L/R} = 10°/30°$. At this same differential strake deflection of 20° for the 0° symmetric strake deflection, the yawing moment reversal was at a maximum. For $\delta_{s,\,L/R} = 10°/30°$, the right forebody/strake vortex suction peak is greater at F.S. 85 than the left but lifts off from the surface sooner, as can be seen by the vortex suction peak pressures at F.S. 142. At F.S.142, the left forebody/strake vortex suction peak at $\theta \approx 190°$ is much larger than on the right at $\theta \approx 160°$ since the right vortex is farther from the surface at that point and has less effect on the surface pressures. The left forebody/strake vortex accelerates the flow around the left side of the fuselage resulting in lower pressures on the left side at F.S. 107 to F.S. 184. Note the strength of the left vortex footprint at $\theta = 200°$ at F.S. 142 and the left and right side pressures as compared to the same for the 0° symmetric strake deployment, $\delta_{s,\,L/R} = 0°/20°$ case (fig. 11(b)). For the same differential strake deflection of 20°, the left forebody vortex had little beneficial effect. In that case, the dominant right forebody/strake vortex caused the flow to accelerate around the right side of the forebody for all stations aft of F.S. 85, increasing those suction pressures and resulting in a yawing moment to the right. On the strakes for $\delta_{s,\,L/R} = 10°/30°$ the suction peak on the inboard right strake surface at F.S. 85, $y/b = 0.85$, is caused by the proximity of the forebody/strake vortex. The outboard strake surface pressures are generally less than the inboard surface pressures with the largest difference on the left side. Both the forebody and strakes pressure integrations result in yawing moments to the left, (figs. 8 and 10(b)).

As supporting evidence of this analysis, for $\alpha = 47°$, $\beta = 0.2°$, and $\delta_{s,\,L/R} = 5°/35°$, figure 14(a) shows the left and right forebody/strake vortices in the wingtip photograph. The right forebody/strake vortex can be seen higher and lifting off the surface sooner. The left vortex stays much closer to the surface and provides the suction needed to accelerate the flow around the left side of the forward fuselage aft of the radome. For comparison, smoke flow visualization is shown in figure 14(b) for the 0° symmetric strake deployment case at $\delta_{s,\,L/R} = 0°/27°$, $\alpha = 50°$, and $\beta = -1.4°$. For nearly the same differential strake position, only the right forebody/strake vortex close to the surface can be seen. The left vortex does not appear to have a core that can be identified from the photograph.

Comparison with Wind Tunnel Results

A similar radome with conformal strakes was tested on an F-18 airplane in the NASA Ames Research Center, Moffett Field, California, 80- by 120-ft Wind Tunnel.[25] This full-scale model had pressure orifices at the same fuselage stations as the HARV. The conformal strakes on this radome, however, did not have the cutouts for the bulkheads that were on the HARV, (fig. 6).

Pressure distributions from flight and wind tunnel at $\alpha = 50°$ and $\delta_{s,\,L/R} = 0°/90°$ are compared in figure 15. The most obvious difference between flight and the wind-tunnel results is the deficit in the suction peak on the left side ($\theta \approx 240°$ to $280°$) starting at F.S. 70 and progressing aft for the flight data. The wind-tunnel data suction peak is much smoother and fuller, similar to previous HARV radome results from flight (fig. 12(a)).[19] The major difference between the wind-tunnel model radome and the ANSER radome was that the large cutouts for the flight ANSER radome were not present on the wind-tunnel model. These cutouts were sealed from the interior of the radome but not sealed between other cutouts. Axial flow from a region of higher pressure to a region of lower pressure could have existed, thereby affecting the suction peaks at F.S. 70, F.S. 85, and F.S. 107.

On the right side of the fuselage, the pressure distributions from flight and wind tunnel showed good agreement at F.S. 70, F.S. 85, and F.S. 107. At F.S. 142 and F.S. 184, however, the suction pressures on the right side from flight are higher than those from the wind tunnel. The net result is that the wind tunnel has higher forebody yawing moment coefficients for this test condition (fig. 6).

CONCLUDING REMARKS

In-flight pressure distributions have been reported at an angle of attack (α) of 50° at five fuselage stations on the F-18 High Alpha Research Vehicle (HARV) forebody with actuated forebody strakes. Forebody yawing moments integrated from the forebody pressures were presented at angles of attack of 20° to 65°. The results have been correlated with in-flight off-surface flow visualization and wind-tunnel data from the NASA Ames Research Center 80-ft by 120-ft Wind Tunnel and the NASA Langley Research Center 30-ft by 60-ft Wind Tunnel.

Forebody strakes can generate large yawing moments at high angles of attack. When one strake is deployed fully open, the maximum forebody yawing moment from flight is approximately one-half of the maximum aircraft yawing moment from the wind tunnels. At $\alpha = 50°$, the flight forebody yawing moment is only approximately 80 percent of the wind-tunnel forebody yawing moment. The peak forebody yawing moment from flight was at $\alpha = 55°$ and at $\alpha = 59°$ (maximum test α) for the wind tunnel. Peak forebody yawing moment for the whole airplane from the wind tunnel was at 50°. At $\alpha = 59°$ for the wind tunnel and 65° for flight, the forebody and total aircraft yawing moments from the wind tunnel were approximately equivalent.

At an angle of attack of 50°, deflecting one strake at a time resulted in a forebody yawing moment control reversal for small strake deflection angles. Deflecting the strakes differentially about a 20° symmetric strake deployment eliminated the control reversal and produced a nearly linear variation of forebody yawing moment with differential strake deflection.

When the forebody yawing moments are broken down into radome and forward fuselage yawing moments at $\alpha = 50°$, the major forebody yawing moment is not generated at the region where the strakes are located but rather at the forebody region behind the strakes. At $|\delta_{s,d}| \leq 30°$, the forward fuselage behind the radome accounts for practically all of the forebody yawing moment.

With the right strake deflections of 20° and left strake retracted at $\alpha = 50°$, the pressure distributions show that the right forebody/strake vortex was close to the surface. This configuration caused the flow to accelerate around the forward fuselage behind the strake, which resulted in lower pressures on the right side and a forebody yawing moment to the right. For right strake deflections of 60°, the right forebody/strake vortex lifted from the surface of the radome and the left forebody vortex grew in strength and stayed close to the surface. This vortex action caused the flow to accelerate around the left side of the forebody, resulting in lower pressures on the left side and hence a yawing moment to the left.

At $\alpha = 50°$ using the 20° symmetric strake deployment with the left strake deflection of 10° and a right strake deflection of 30°, the deflected left strake increased the strength of the left forebody/strake vortex. This vortex was also closer to the surface than the right forebody/strake vortex and accelerated the flow around the left side, resulting in lower pressures on the left side for all conditions and a forebody yawing moment to the left with no forebody yawing moment control reversal.

A deficit in the suction peaks of the flight pressure distributions was noted just below the undeflected strake as compared to the original HARV radome data and to the wind-tunnel radome data. This deficit was possibly caused by the cutouts in the strakes required for the fuselage bulkheads on the flight hardware.

REFERENCES

[1] Chambers, Joseph R., "High-Angle-of-Attack Technology: Progress and Challenges," *High Angle-of-Attack Technology Conference*, NASA-CP-3149, vol. 1, pt. 1, 1990, pp. 1–22.

[2] Bowers, Albion H. and Pahle, Joseph, "The High Alpha Research Vehicle," *High Angle of Attack Conference*, NASA Langley Research Center, September 1996.

[3] Chambers, Joseph R., Gilbert, William P., and Nguyen, Luat T., *High-Angle-of-Attack Technology*, vol. 1, pt. 1–3, NASA-CP-3149, 1990.

[4] *High-Angle-of-Attack Projects and Technology Conference*, compiled by Neil W. Matheny, NASA-CP-3207, vol. 1–4, 1992.

[5] *Fourth High Alpha Conference*, NASA-CP-10143, vol. 1–3, July 1994.

[6] *High-Angle-of-Attack Technology, Accomplishments, Lessons Learned, and Future Directions*, compiled by Joseph R. Chambers, James R. Burley, II and Robert R. Meyer, Jr., NASA CP-1998-207676, June 1998.

[7] Asbury, Scott C. and Capone, Francis J., *Multiaxis Thrust-Vectoring Characteristics of a Model Representative of the F-18 High Alpha Research Vehicle at Angles of Attack from 0° to 70°*, NASA TP-3531, 1995.

[8] Murri, Daniel G., Biedron, Robert T., Erickson, Gary E., Jordan, Frank L., Jr., and Hoffler, Keith D., "Development of Actuated Forebody Strake Controls for the F-18 High Alpha Research Vehicle," *High Angle-of-Attack Technology Conference*, NASA CP-3149, vol. 1, pt. 1, 1990, pp. 335–380.

[9] Biedron, Robert T. and Thomas, James L., "Navier-Stokes Computations for an F-18 Forebody with Actuated Control Strake," *High Angle-of-Attack Technology Conference*, NASA-CP-3149, vol. 1, pt. 1, 1990, pp. 481–506.

[10] Lanser, Wendy R. and Meyn, Larry A., "Forebody Flow Control on a Full-Scale F/A-18 Aircraft," *J. of Aircraft*, vol. 31, no. 6, 1994, pp. 1365–1371.

[11] Lanser, Wendy R. and Murri. Daniel G., "Wind Tunnel Measurements on a Full-Scale F/A-18 with Forebody Slot Blowing or Forebody Strakes," AIAA 93-1018, 1993.

[12] Pahle, Joseph, Foster, John, Bundick, Tom, and Wichman, Keith, "An Overview of Controls and Flying Qualities Technology on the F/A-18 High Alpha Research Vehicle," *High-Angle-of-Attack Technology, Accomplishments, Lessons Learned, and Future Directions*, NASA CP-1998-207676/PT 1, June 1998, pp. 193–219.

[13] Hancock, Regis and Fullerton, Gordon, "X-29 Vortex Flow Control Tests," *Society of Experimental Test Pilots 1992 Report to the Aerospace Profession, 36th Symposium Proceedings*, 1992, pp. 209–219.

[14] Walchli, Lawrence A., "Flight Evaluation of Pneumatic Forebody Vortex Control in Post-Stall Flight," *Fourth High Alpha Conference*, NASA CP-10143, vol. 3, 1994.

[15] Murri, Daniel G., and Rao, Dhanvada M., "Exploratory Studies of Actuated Forebody Strakes for Yaw Control at High Angles of Attack," AIAA 87-2557, 1987.

[16] Murri, Daniel G., Shah, Gautam H., DiCarlo, Daniel J., and Trilling, Todd W., "Actuated Forebody Strake Controls for the F-18 High-Alpha Research Vehicle," *J. of Aircraft*, vol. 32, no. 3, 1995, pp. 555–562.

[17] Fisher, David F., Daniel G. Murri and Wendy R. Lanser, *Effect of Actuated Forebody Strakes on the Forebody Aerodynamics of the NASA F-18 HARV*, NASA TM-4774, October 1996.

[18] Moes, Timothy R. and Whitmore, Stephen A., *A Preliminary Look at Techniques Used to Obtain Airdata From Flight at High Angles of Attack*, NASA TM-101729, 1990.

[19] Fisher, David F., Banks, Daniel W., and Richwine, David M., *F-18 High Alpha Research Vehicle Surface Pressures: Initial In-Flight Results and Correlation with Flow Visualization and Wind-Tunnel Data*, NASA TM-101724, 1990.

[20] Curry, Robert E. and Richwine, David M., "An Airborne System for Vortex Flow Visualization on the F-18 High-Alpha Research Vehicle," *AIAA/NASA/AFWAL Sensors and Measurements Technology Conference*, 88-4671-CP, Atlanta, Georgia, September 7–9, 1988.

[21] Fisher, David F., Del Frate, John H., and Richwine, David M., *In-Flight Flow Visualization Characteristics of the NASA F-18 High Alpha Research Vehicle at High Angles of Attack*, NASA TM-4193, 1990.

[22] Fisher, David F. and Lanser, Wendy R., "Flight and Full-Scale Wind-Tunnel Comparison of Pressure Distributions From an F-18 Aircraft at High Angles of Attack," *Fourth High Alpha Conference*, NASA CP-10143, vol. 1, 1994.

[23] Whitmore, Stephen A. and Moes, Timothy R., "The Effects of Pressure Sensor Acoustics on Airdata Derived from a High Angle-of-Attack Flush Airdata Sensing (HI-FADS) System," AIAA 91-0671, January 1991.

[24] Murri, Daniel G., Fisher, David F., and Lanser, Wendy R., "Flight-Test Results of Actuated Forebody Strake Controls on the F-18 High-Alpha Research Vehicle," *High-Angle-of-Attack*

Technology, Accomplishments, Lessons Learned, and Future Directions, NASA CP-1998-207676, pt. 2, June 1998, pp. 881–929.

[25]Lanser, Wendy R., Meyn, Larry A., Botha, Gavin A., Ross, James C., James, Kevin D., Hall, Robert M., Murri, Daniel G., and Shah, Gautam H., "Overview of Full-Scale F/A-18 Tests in the 80- by 120-ft Wind Tunnel with Small-Scale Comparisons," *High-Angle-of-Attack Technology, Accomplishments, Lessons Learned, and Future Directions*, NASA CP-1998-207676, pt. 2, June 1998, pp. 745–770.

[26]Fisher, David F. and Cobleigh, Brent R., *Controlling Forebody Asymmetries in Flight–Experience with Boundary Layer Transition Strips*, NASA TM-4595, 1994. (see also AIAA-94-1826, July 1994.).

FIGURES

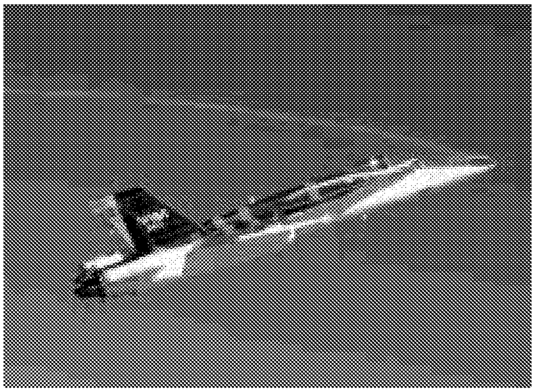

EC96 45540-29

Figure 1. F-18 HARV aircraft with ANSER radome, $\alpha \approx 30°$, $\delta_{s,\,L/R} = 0°/90°$.

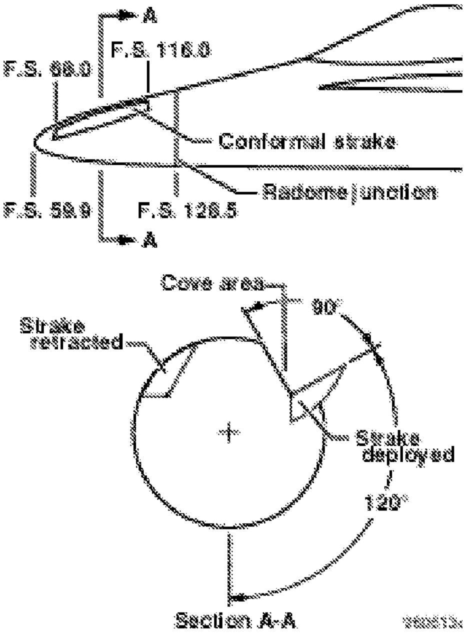

Figure 2. Sketch of forebody strakes on the F-18 HARV.

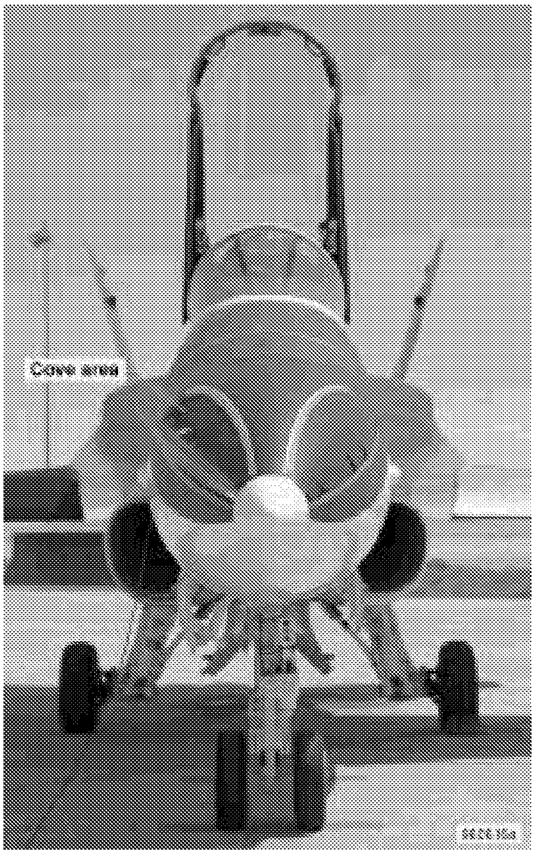

Figure 3. F-18 HARV with ANSER radome and right forebody strake deployed.

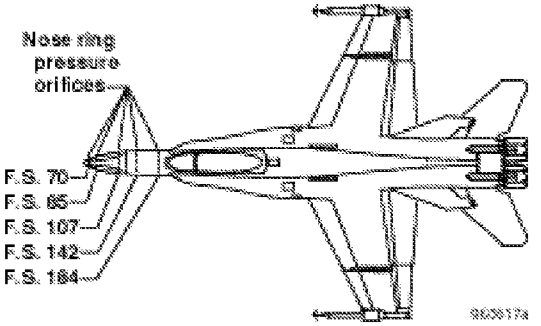

Figure 4. Location of pressure orifices on F-18 HARV forebody.

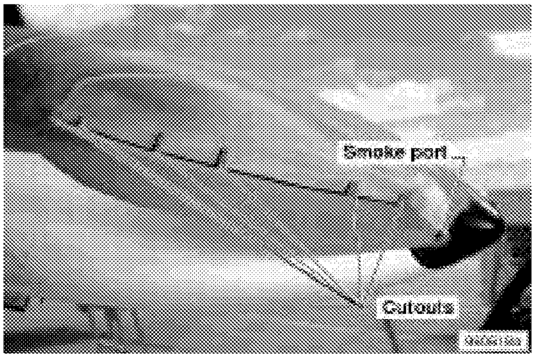

Figure 5. Close-up of right smoke port and strake cutouts on ANSER radome.

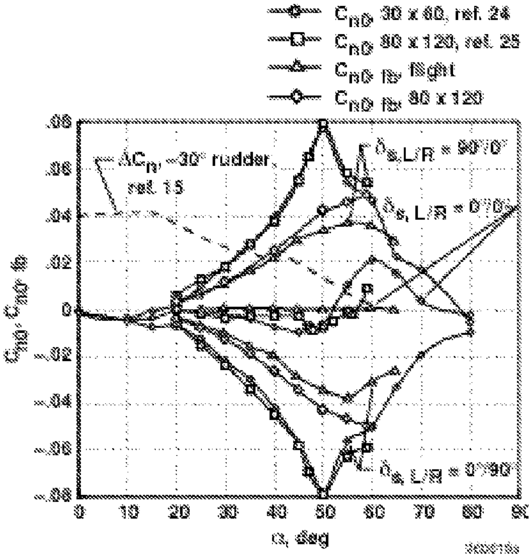

Figure 6. Comparison of forebody yawing moments from flight and wind tunnel and total aircraft yawing moments from wind tunnel.

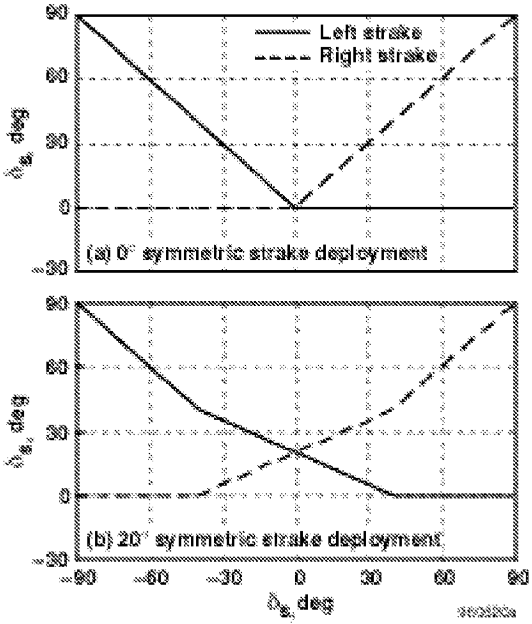

Figure 7. Symmetric strake deployment schedule.

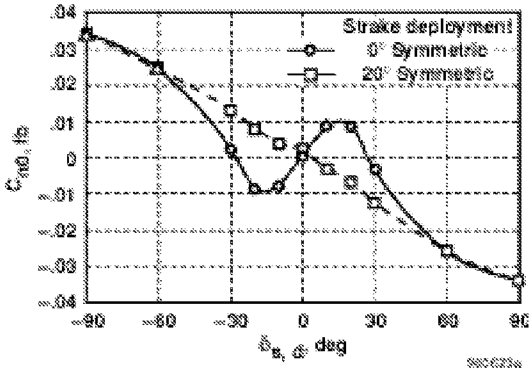

Figure 8. F-18 HARV forebody yawing moments as a function of differential strake position, $\beta = 0°$.

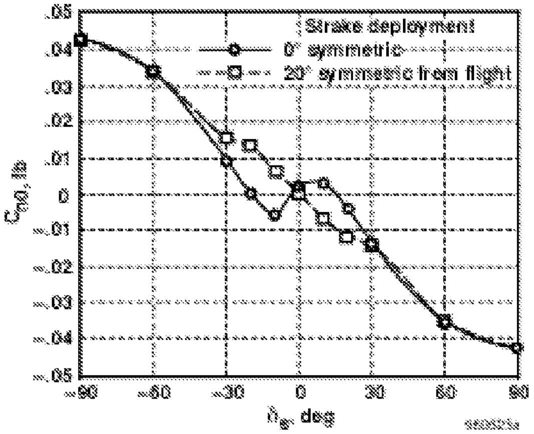

Figure 9. 80- by 120-ft Wind Tunnel forebody yawing moments as a function of differential strake position, β = 0°, $\alpha = 50$ °, and 0° symmetric from flight.

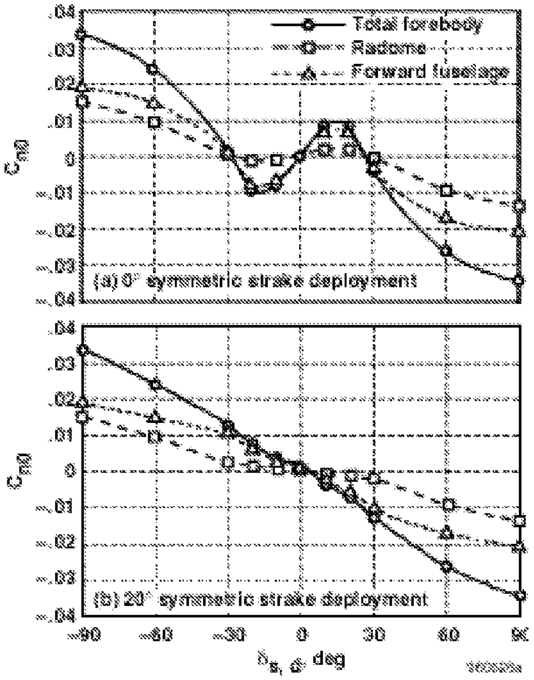

Figure 10. F-18 HARV forebody, radome, and forward fuselage yawing moments as a function of differential strake position, $\alpha = 50°$ and $\beta = 0°$.

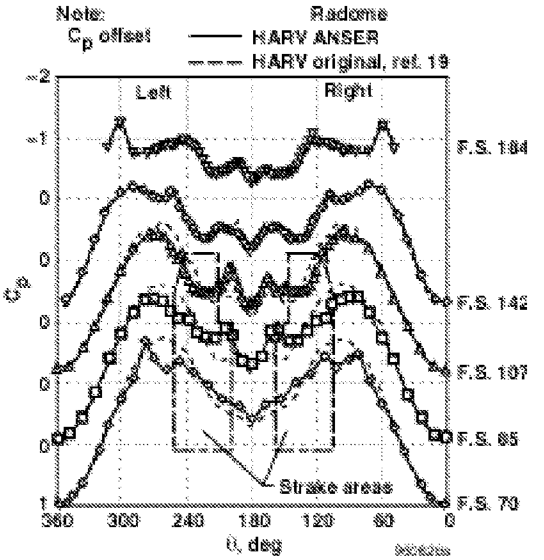

(a) $\delta_{s,\ L/R}$ = 0°/0° with comparison to previous flight results, M = 0.27, $Re_c = 9.2 \times 10^6$.

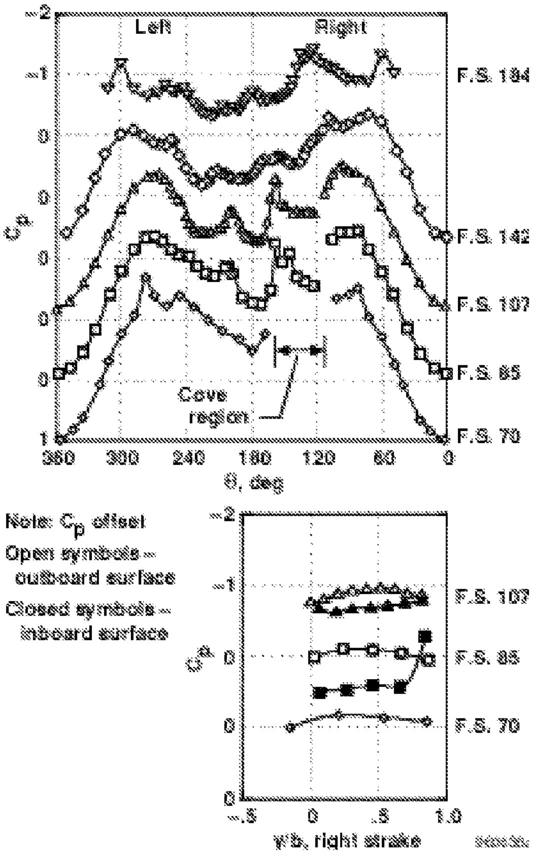

(b) $\delta_{s,\ L/R}$ = 0°/20°, M = 0.26, $Re_c = 9.8 \times 10^6$.

Figure 11. Forebody and strake pressure distributions with the ANSER radome at

$\alpha = 50°$ for the 0° symmetric strake deployment, pilot's view.

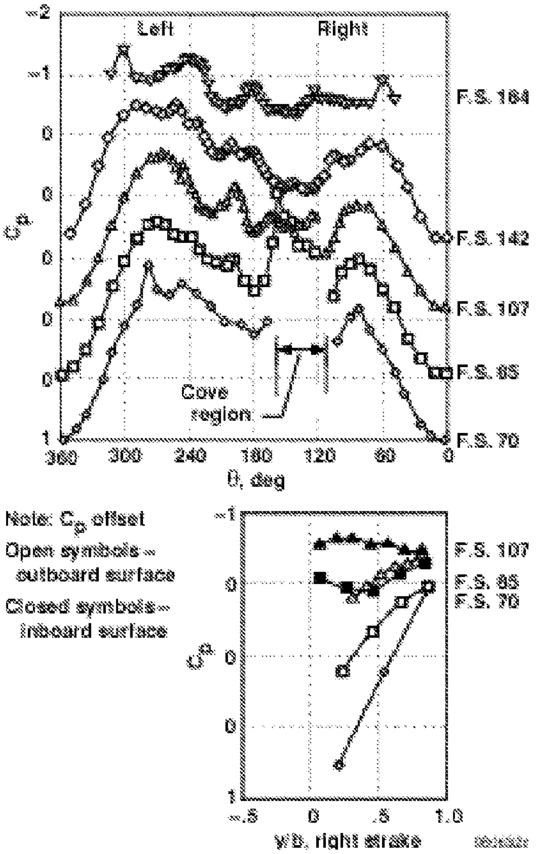

(c) $\delta_{s,\,L/R} = 0°/60°$, M = 0.26, $Re_c = 9.3 \times 10^6$.

Figure 11. Continued.

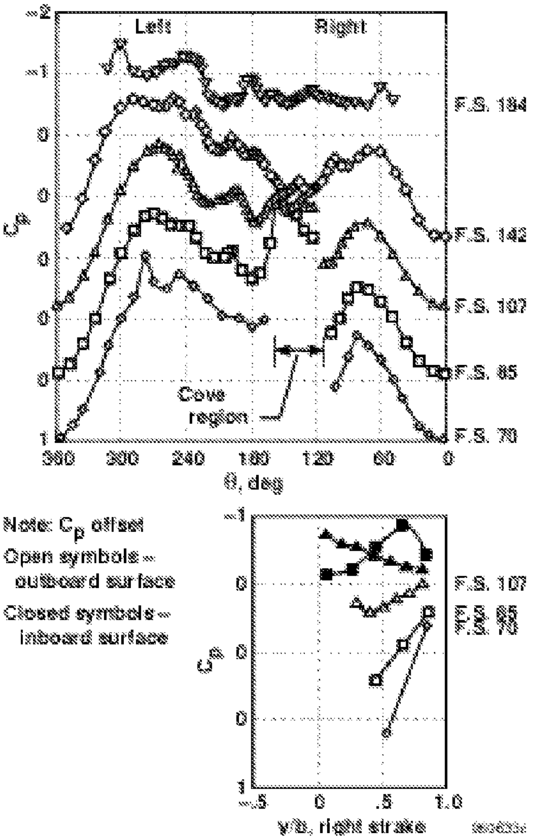

(d) $\delta_{s,\,L/R} = 0°/90°$, M = 0.24, $Re_c = 9.4 \times 10^6$.

Figure 11. Concluded.

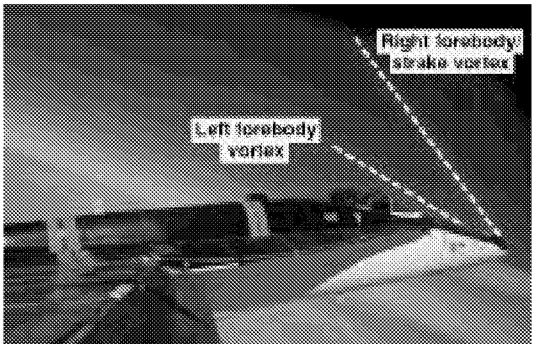

Figure 12. Forebody/strake vortex flow visualization for $\alpha = 50°$ and $\delta_{s,\,L/R} = 0°/90°$.

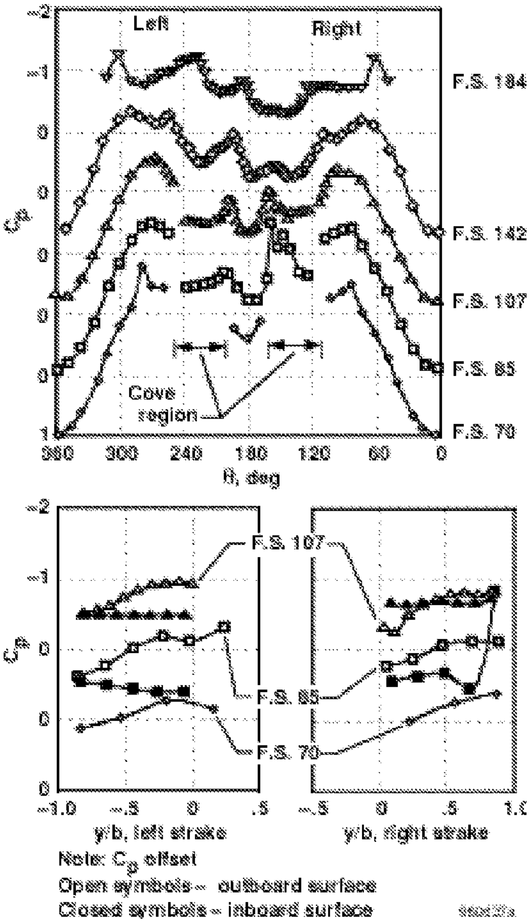

Figure 13. Forebody and strake pressure distributions with the ANSER radome at $\alpha = 50°$ for the 20° symmetric strake deployment, pilot's view, $\delta_{s,\,L/R}$ = 10°/30°, M = 0.28, $Re_c = 10.2 \times 10^6$.

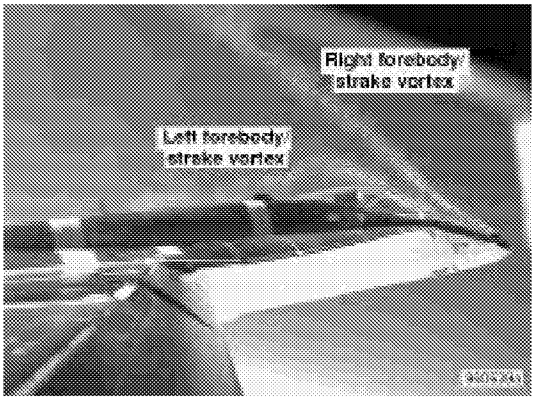

(a) $\delta_{s,\,L/R}$ = 5°/35°.

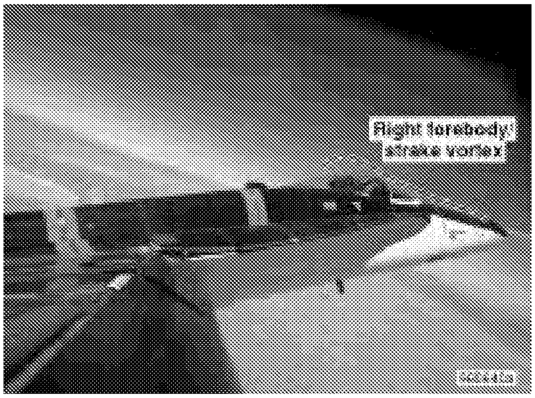

(b) $\delta_{s,\,L/R}$ = 0°/27°.

Figure 14. Forebody/strake vortex flow visualization for α = 50° and $\delta_{s,d} \approx$ 30°.

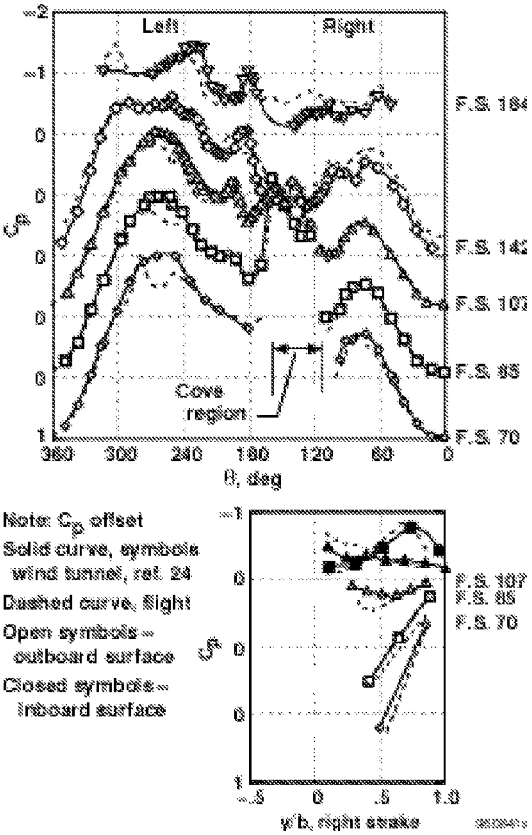

Figure 15. Comparison of flight and wind tunnel pressure distributions, α = 50°, $\delta_{s,\,L/R} = 0°/90°$, M = 0.24, $Re_c = 9.4 \times 10^6$.

REPORT DOCUMENTATION PAGE

Form Approved
OMB No. 0704-0188

1. AGENCY USE ONLY (Leave blank)

2. REPORT DATE
May 2001

3. REPORT TYPE AND DATES COVERED
Conference Paper

4. TITLE AND SUBTITLE
Forebody Aerodynamics of the F-18 High Alpha Research Vehicle With Actuated Forebody Strakes

5. FUNDING NUMBERS
WU 710-55-04-E8-RR-00-000

6. AUTHOR(S)
David F. Fisher and Daniel G. Muri

7. PERFORMING ORGANIZATION NAME(S) AND ADDRESS(ES)
NASA Dryden Flight Research Center
P.O. Box 273
Edwards, California 93523-0273

8. PERFORMING ORGANIZATION REPORT NUMBER
H-2447

9. SPONSORING/MONITORING AGENCY NAME(S) AND ADDRESS(ES)
National Aeronautics and Space Administration
Washington, DC 20546-0001

10. SPONSORING/MONITORING AGENCY REPORT NUMBER
MP-69-P-45

11. SUPPLEMENTARY NOTES
Presented at the Symposium on Advanced Flow Management, Loen, Norway, May 7—10, 2001.

12a. DISTRIBUTION/AVAILABILITY STATEMENT
Unclassified—Unlimited
Subject Category 02

12b. DISTRIBUTION CODE

13. ABSTRACT (Maximum 200 words)

Extensive pressure measurements and off-surface flow visualization were obtained on the forebody and strakes of the NASA F-18 High Alpha Research Vehicle (HARV) equipped with actuated forebody strakes. Forebody yawing moments were obtained by integrating the circumferential pressures on the forebody and strakes. Results show that large yawing moments can be generated with forebody strakes. At a 50°-angle-of-attack, deflecting one strake at a time resulted in a forebody yawing moment control reversal for small strake deflection angles. However, deflecting the strakes differentially about a 20° symmetric strake deployment eliminated the control reversal and produced a near linear variation of forebody yawing moment with differential strake deflection. At an angle of attack of 50° and for 0° and 20° symmetric strake deployments, a larger forebody yawing moment was generated by the forward fuselage (between the radome and the apex of the leading-edge extensions) than on the radome where the actuated forebody strakes were located. Cutouts on the flight vehicle strakes that were not on the wind tunnel models are believed to be responsible for deficits in the suction peaks on the flight radome pressure distributions and differences in the forebody yawing moments.

14. SUBJECT TERMS
Aircraft, F-18, Flight, Flight Test, Flow visualization, Forebody, Smoke, Strake, Vortex, Vortical flow

15. NUMBER OF PAGES
16

16. PRICE CODE
A03

17. SECURITY CLASSIFICATION OF REPORT
Unclassified

18. SECURITY CLASSIFICATION OF THIS PAGE
Unclassified

19. SECURITY CLASSIFICATION OF ABSTRACT
Unclassified

20. LIMITATION OF ABSTRACT
Unlimited